

Onsager Condensation in Chiral Active Matter: Universality of Supersonic Topological Gas Dynamics

Magnus F Ivarsen*

Department of Physics and Engineering Physics, University of Saskatchewan, Saskatoon, Canada

To explain how dissipative active turbulence sustains inertial cascades, we construct a chiral model mapping overdamped agents to supersonic topological gas dynamics. Here, Mach cones function as acoustic horizons, shielding defect cores from the sound radiation of shallow water flows. We show that disorder activates a topological heat pump driving an inverse cascade toward a negative-temperature Onsager dipole, unless arrested into a vortex glass by insufficient dispersion. This mapping identifies a universality class unifying active swarms with the statistical mechanics of classical inviscid fluids.

INTRODUCTION

Active turbulence, the chaotic spatiotemporal dynamics observed in bacterial swarms [1, 2], cytoskeletal extracts [3], and synthetic colloidal flocks [4, 5], presents a challenge to statistical physics. Unlike classical inertial turbulence, which is driven by high Reynolds numbers (Re), active turbulence arises in the overdamped limit ($Re \approx 0$), driven by the continuous injection of energy at the microscale [6, 7].

Despite the viscous dominance in such systems, observations frequently reveal large-scale coherent structures reminiscent of inertial fluid flows [8]. This has ignited a debate regarding the universality class of active matter [3]. Current theories, largely built on the hydrodynamics of *active nematics* [9], predict steep energy spectra (typically $E(k) \sim k^{-4}$ or k^{-3}) dominated by the proliferation of half-integer defects [10, 11]. While such models successfully describe transient pattern formation, they generally fail to predict the robust inverse energy cascades ($k^{-5/3}$) observed in chiral active fluids [12] and 2D quantum turbulence [13].

Though active matter systems frequently and demonstrably exhibit viscous, dissipative turbulence [14–16], the observational discrepancy implies a missing link in the theoretical framework. While odd viscosity enables unidirectional flow [17, 18] and recent models suggest swarming can be entropy-driven [19], the thermodynamic end-state of such systems remains largely unexplored. Specifically, does the breaking of detailed balance [20] by intrinsic rotation sustain a chaotic steady state, or can it drive the system toward a specific macroscopic attractor?

In this letter, we propose that the answer to the conundrum lies in treating such systems as topological gases. By simulating chiral active matter as an ensemble of N locally phase-coupled oscillators experiencing a Kuramoto-like phase-interaction [21], we demonstrate that active turbulence can exhibit a duality; a microscopic active bath dominated by enstrophy injection can simultaneously be described as a macroscopic renormalised fluid governed by the conservative advection of topological defects. By filtering out the microscopic singularities, we reveal that the simulated system

undergoes a “hidden” inverse energy cascade, indistinguishable from Euler (frictionless, inviscid) turbulence. This cascade functions akin to a thermodynamic pump, driving the system toward an *Onsager dipole*, a negative-temperature condensate of vorticity [22], thereby unifying the phenomenology of biological swarms with the rigorous statistical mechanics of point vortices.

METHODOLOGY

The Model We define the system as a chiral active fluid composed of $N = 50,000$ particles, or discrete agents, in a bounded periodic domain $\mathcal{D} \in \mathbb{R}^2$. The state of the i^{th} agent is defined by its position $\mathbf{r}_i(t)$ and its internal phase $\phi_i(t) \in [0, 2\pi]$. The agents do not interact via pairwise collisions (as in granular matter) but through a local mean field. Following Ref. [21], we define the complex order parameter field $Z(\mathbf{r}, t)$ as the convolution of the microscopic agent distribution with a finite-range interaction kernel G :

$$Z(\mathbf{r}, t) = R(\mathbf{r}, t) e^{i\Psi(\mathbf{r}, t)} = \int_{\mathcal{D}} G(|\mathbf{r} - \mathbf{r}'|) \left[\sum_{j=1}^N \delta(\mathbf{r}' - \mathbf{r}_j(t)) e^{i\phi_j(t)} \right] d\mathbf{r}', \quad (1)$$

where $G(|\mathbf{r} - \mathbf{r}'|)$ is the Green’s function of the interaction (modeled as a Gaussian with kernel size σ), $R(\mathbf{r}, t)$ is the local coherence (or order parameter, where $R \approx 1$ implies high local synchronisation and $R \approx 0$ implies a phase singularity, or defect core). $\Psi(\mathbf{r}, t)$ is the local mean phase. The convolution kernel G is interpreted in the context of chemical gradients or electric fields, which govern the dense active matter interactions (e.g., bacterial swarms). By modifying G , we can potentially simulate anisotropic media (like magnetized plasmas) without changing the agent logic.

Following Ref. [21], the internal phase ϕ_i evolves according to an overdamped, localized, driven Kuramoto-Sakaguchi-like interaction [23, 24]:

$$\dot{\phi}_i = \underbrace{\omega_i}_{\text{Driver}} + \underbrace{a_0 R(\mathbf{r}_i) \sin(\Psi(\mathbf{r}_i) - \phi_i)}_{\text{Synchronisation force}} + \underbrace{\eta_i(t)}_{\text{Noise}}, \quad (2)$$

where ω_i are natural frequencies drawn from a power-law distribution $P(\omega) \sim \omega^{-n}$, a_0 is the coupling Strength, η_i

is a Gaussian white noise term (amplitude 0.15), and $n = 1.5$ is a positive constant of order unity to facilitate the non-linear transfer of energy (see Refs. [21, 25]). R_i , the local order parameter, ensures that synchronisation is triggered by initially random local alignments in phase. ω_i (and the stochastic term η_i) prevent a “ferromagnetic collapse”, in which the system simply synchronises globally ($\phi_i = \text{const}$) causing a uniform ballistic drift. By forcing the particles to oscillate with an inherent frequency (or attempt to do so), the ω_i terms act as frustration, constantly injecting vorticity at the micro-scale, which, as we shall demonstrate, feeds an inverse energy cascade.

The definitive equation of this model, distinguishing it from standard fluids, is the agent-based, non-inertial slave principle, where the velocity vector is explicitly determined by the instantaneous phase:

$$\dot{\mathbf{r}}_i = \mathbf{v} = v_0(\cos \phi_i, \sin \phi_i), \quad (3)$$

where v_0 is the active swim speed and $\mathbf{r}_i = (x_i, y_i)$. The particles are therefore without conventional inertia: $\sum \mathbf{F} \neq m\mathbf{a}$; the system is fully overdamped, in a low Reynolds number limit [26]. The velocity field naturally forms vortices, introducing singularities, and so to define a valid continuum fluid, we introduce the renormalised fluid element (RFE), which we motivate theoretically in the Supplementary Materials.

At this point, we identify the characteristic scales in our model; the kernel size σ and the active swim speed v_0 , which yield the interaction time $\tau \equiv \sigma/v_0 = (3 \text{ grid units})/(0.5 \text{ grid units/s}) = 6 \text{ s}$, yielding the dimensionless units $\tilde{x} = x/\sigma$, $\tilde{t} = t/\tau$, and $\tilde{\omega} = \omega(\sigma/v_0)$ (we subsequently drop the tilde). The system size becomes $\Lambda = 2L/\sigma \approx 13$. A natural definition of the RFE is then afforded by τ ; we define the RFE as the center of mass of a particle’s trajectory during τ , effectively course-graining the singularities:

$$r_i^{\text{RFE}} = \text{angle} \left(\frac{1}{\tau} \sum_{t'=\tau}^t \hat{r}_i(t') \right) \cdot \frac{\Lambda}{\pi}, \quad (4)$$

with $\hat{r}_i(t)$ being,

$$\hat{r}_i(t) = \exp \left(i \cdot \frac{r_i(t)}{\Lambda} \cdot \pi \right), \quad (5)$$

being the complex phasor locations mapped to a unit circle (necessitated by the periodic boundary conditions). The transformation Eqs. (4, 5) constitute the regularization of the topological defects in ϕ_i , which become physical flow vortices in \mathbf{r}_i .

The correlation wavenumber of the local mean field is $k_c = 2\pi/\sigma$, or simply 2π with normalized units, establishing a natural scale separation that marks the transition between the microscopic active bath ($k > k_c$) and the macroscopic hydrodynamic limit ($k < k_c$), with k being

the normalized wavenumber. The RFE operator effectively acts as a low-pass filter with cut-off k_c .

Theoretical foundation To bridge the discrete dynamics and the continuum fluid, we present, in the Supplementary Materials, a rigorous derivation proving that the dynamics produced by the model equations (Eqs. 1–5) are isomorphic to shallow water hydrodynamics with topography. A brief summary follows.

By decomposing the particle velocity into a mean flow with fluctuations, we find that the macroscopic velocity \mathbf{u} is governed by the mean phase gradient $\nabla \Psi$ scaled by the local order parameter R : $\mathbf{u} \approx R \nabla \Psi$. While we derive a set of constraining equations that are isomorphic to shallow water hydrodynamics, there are striking differences: the effective inertial mass in our model scales with order:

$$\lambda = R^2, \quad (6)$$

with an effective restoring potential (enthalpy),

$$h_{\text{eff}} = \frac{v_0^2}{2} R^2. \quad (7)$$

The macroscopic restoring force is governed by the Eq. (7)’s gradient, enforcing a sound speed that is also proportional to order,

$$c_s = \frac{v_0 R}{\sqrt{2}}. \quad (8)$$

Since the inertial velocity *likewise* scales with R , this locks the flow into an inherently supersonic state (Mach number > 1). Consequently, defect cores ($R \rightarrow 0$) are isolated behind Mach cones, creating sonic horizons that prevent radiative decay. While fast compressible shocks disperse inertial energy locally, the time-averaged background flow remains incompressible. This effectively traps energy within the topological degrees of freedom, meaning the macroscopic dynamics are governed strictly by the conservation of topological charge.

As the mean field $\Psi(r)$ is the argument of a single-valued complex field (Eq. 1), its circulation along any closed loop $\partial\Sigma$ enclosing a defect core is necessarily quantized [27, 28], mirroring the winding number stability in discrete oscillator ensembles [21, 29]:

$$\oint_{\partial\Sigma} \nabla \Psi \cdot d\mathbf{l} = 2\pi m. \quad (m \in \mathbb{Z}) \quad (9)$$

Thus, the interaction energy of the ensemble is given by the Kirchhoff-Onsager Hamiltonian [30, 31]:

$$H = - \sum_{i \neq j} \Gamma_i \Gamma_j \ln |\mathbf{r}_i - \mathbf{r}_j|. \quad (10)$$

This Hamiltonian confirms that while individual agents are overdamped, the renormalised fluid behaves as an inviscid point-vortex gas of topological defects on long timescales.

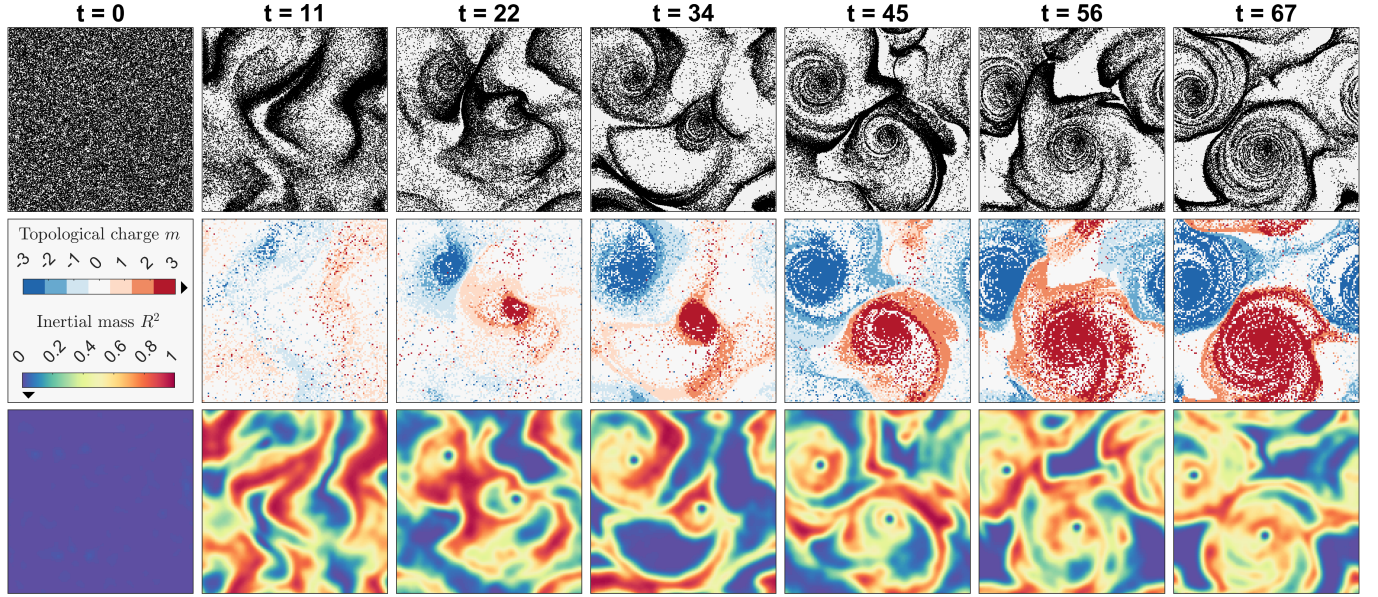


FIG. 1. The emergence of the Onsager dipole in simulated chiral active matter, shown in seven temporal snapshots of the simulation space. The top row shows the RFE particle point-clouds r_i^{RFE} , the middle row shows topological charge m , and the bottom row shows inertial mass R^2 , using the colorscales indicated.

The dynamic Onsager attractor In a bounded domain \mathcal{D} , the phase space volume $\Omega(E)$ eventually decreases as energy increases, implying a negative temperature regime ($T < 0$) where entropy favors the merging of like-signed vortices [22]. However, in our active chiral matter model, the dipole is continuously eroded by supersonic shocks which thermalise inertial energy back into the active bath. Consequently, the Onsager dipole emerges as a *dynamic attractor*, where an active bath constantly rebuilds topological order using newly thermalised energy, sustaining the system in the negative-temperature Onsager regime. Crucially, the mechanism parallels observed inverse-energy cascades [1], motility-induced phase separation [32], and entropy-driven ordering [19] in active matter studies.

Spectral scaling This framework predicts a spectral dichotomy based on the scale of observation. At the microscopic scale, the raw particle field is dominated by the singular geometry of the phase defects ($\nabla\phi \sim 1/r$), forcing the system into the enstrophy-dominated regime with a steep spectral index $E_{\text{raw}}(k) \sim k^{-3}$ [33–36]. Conversely, the macroscopic dynamics are governed by the Kirchhoff-Onsager Hamiltonian (Eq. 10), which describes an effective inviscid (frictionless) fluid. The RFE field, which filters out the microscopic singularities, will therefore recover the classical inverse energy cascade signature, exhibiting the Kolmogorov scaling $E_{\text{RFE}}(k) \sim k^{-5/3}$ [13, 37]. The renormalization unifies the dissipative phenomenology of active matter with the conservative statistical mechanics of Euler fluids.

We quantify the non-linear transfer of energy across scales using the standard spectral flux $\Pi(k)$, defined via

the advective transport term $(\mathbf{v} \cdot \nabla)\mathbf{v}$ characteristic of fluid turbulence,

$$\Pi(k) = - \int_0^k T(k') dk', \quad (11)$$

where the energy transfer function $T(k)$ is defined for a velocity field \mathbf{v} as [39],

$$T(k) = \sum_{|\mathbf{q}|=k} \text{Re} \left[\hat{\mathbf{v}}_{\mathbf{q}}^* \cdot \mathcal{F} \{ -(\mathbf{v} \cdot \nabla) \mathbf{v} \}_{\mathbf{q}} \right], \quad (12)$$

which sums contributions of all discrete wave vectors $\mathbf{q} = (q_x, q_y)$ that fall within the annular shell where the magnitude $|\mathbf{q}| \approx k$, to the real part of the Fourier transform of the advective transport term, where $\hat{\mathbf{v}}_{\mathbf{q}}^*$ is the complex conjugate of the velocity field in Fourier space at wave vector \mathbf{q} . A negative plateau in $\Pi(k)$ will conclusively demonstrate an inverse cascade.

RESULTS

The temporal evolution of the system, shown in Figure 1, reveals a spontaneous transition from microscopic chaos ($t = 0$) to macroscopic order ($t = 11$), as small-scale phase defects nucleate and annihilate rapidly. Surviving defects begin to cluster and merge, forming a sloshing, large-scale dipole ($t = 22$ and beyond).

To discern the mechanism driving this dynamic condensation, we analyzed the kinetic pathways of the topological defects (Figure 2b), the decay of the defect number density $N_d(t)$. Adherence to the theoretical $t^{-0.75}$ scaling [38, 40], distinct from the diffusive t^{-1} rate, confirms that vortex merger is governed by dispersive shock

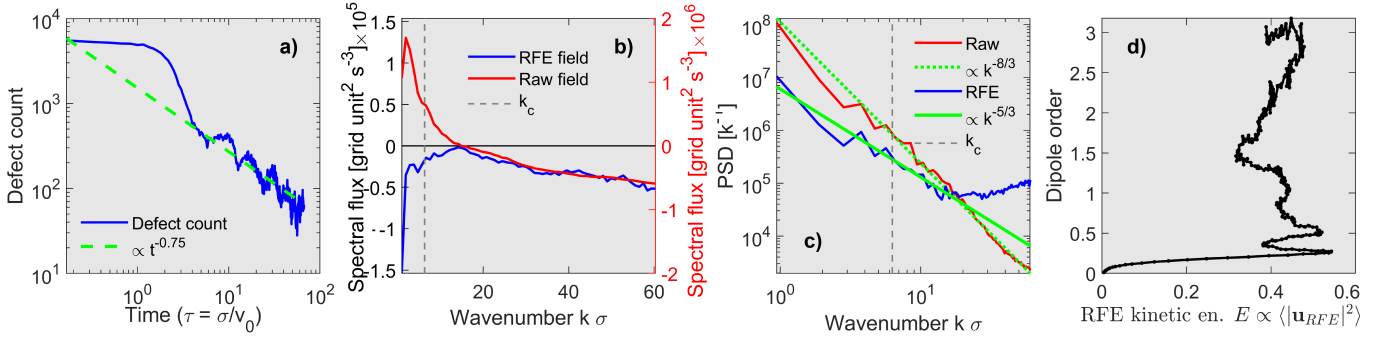


FIG. 2. **Energy characteristics of the simulation run in Figure 1.** **Panel a)** shows the defect (phase singularity) count, with a $t^{-0.75}$ powerlaw scaling [38] shown with a dashed, green line. **Panel b)** shows the spectral flux (Eq. 11) for the RFE (blue, left y -axis) and raw (red, right y -axis) fields, taking the median of the entire simulation. **Panel c)** shows the energy spectrum $E(k)$ for the RFE (blue) and raw (red) fields; a spectral scaling of $k^{-5/3}$ and $k^{-8/3} \approx k^{-2.67}$ is indicated with dotted and solid green lines respectively, and k_c is indicated with a dashed, grey line, as in Panel b). **Panel d)** shows the thermodynamic trajectory, plotting order versus coarse-grained kinetic energy for the simulation evolution.

dynamics [40–42] and acoustic horizons [43], rather than passive strain fields or random-walk annihilation [44].

The directionality of the energy transfer is established by the spectral energy flux $\Pi(k)$ (Figure 2c), where the distinct negative plateau in the spectral flux ($\Pi(k) < 0$) rigorously proves the inverse directionality of the energy cascade; energy injected at the microscale by ω_i is transported to the box size, creating the Onsager dipole.

A central finding of this work is the resolution of the spectral dichotomy observed in active matter, namely the coexistence of steep, dissipative spectra with large-scale coherent structures [13, 45, 46]. Figure 2d) shows that raw particle velocity field exhibits a steep spectral slope consistent with dissipative enstrophy [33]. This reflects the singular geometry of the topological defects: the raw agents are kinematically pinned to the sharp cusps of the phase field ($\nabla\phi \sim 1/r$), and thus their spectrum measures the packing of vorticity filaments [47]. However, when we apply the RFE operator to the ensemble, filtering out the microscopic singularities by averaging over the interaction scale τ , a “hidden” Kolmogorov scaling is revealed: The RFE spectrum $E_{RFE}(k)$ (the blue spectrum in Figure 2d) tracks the classical $k^{-5/3}$ slope characteristic of 2D inviscid fluid turbulence.

Finally, we demonstrate that the formation of the dipole is a thermodynamic inevitability. Figure 2d) maps the system’s trajectory in the energy-order phase plane (E vs. P). The system climbs away from the disordered origin (random gas), increasing both its macroscopic kinetic energy and its dipole order parameter P , while the fluctuations in Figure 2d) reflect the dynamic shock merger mechanism. In the context of Eq. (10), we observe an ascent up the entropy curve into the regime of negative absolute temperature [22]. In the active bath, intrinsic disorder (ω_i) continuously injects enstrophy to maximize the entropy of the renormalised fluid, forcing the long-term spectral condensation of vorticity as the only accessible maximum-entropy state within the bounded

domain. The negative spectral flux in Figure 2b) confirms our hypothesis that the modeled particles act as a dissipative kinetic layer that drives a superfluid governed by the conservative Kirchhoff-Onsager Hamiltonian, unifying the phenomenology of chiral active matter with the rigorous statistical mechanics of classical inviscid fluids.

DISCUSSION

Our results resolve a spectral paradox [4, 48–50] by demonstrating that chiral active matter may exhibit a fundamental scale-dependent duality. At microscopic scales ($k > k_c$), the modeled system is dominated by phase singularities, with a steep spectral slope [33–36]; in our model, this is not a signature of dissipation, but of enstrophy injection; that is, the conversion of intrinsic chemical energy (ω_i) into topological charge.

At macroscopic scales ($k < k_c$), the system reveals a renormalised fluid. By filtering out the singular defects via the RFE operator (Eqs. 4, 5 in empirical terms, Eq. 13 in theoretical terms), we recover an inverse cascade (Figure 2b). The collective motion of the defects generates a “phantom inertia,” an effective advective term, $R(\mathbf{v} \cdot \nabla)\mathbf{v}$ producing dynamics that are isomorphic with shallow water theory (see the Supplementary Materials), despite the overdamped nature of the individual agents.

The thermodynamic trajectory (Figure 2d) takes the system to the inevitable Onsager dipole, confirming that the system continuously maximizes its macroscopic entropy by climbing the energy ladder into the regime of negative absolute temperature [22].

Crucially, the RFE framework suggests a general resolution for the non-universal spectra frequently reported in biological and active matter experiments [10]. We propose that the sharp deviations from Kolmogorov scaling observed in bacterial swarms, active nematics, and cytoskeletal gels [1, 3, 7, 10, 11, 51] may be artifacts of analyzing the raw particle fields rather than the renormalised hydrodynamic modes. By applying the RFE op-

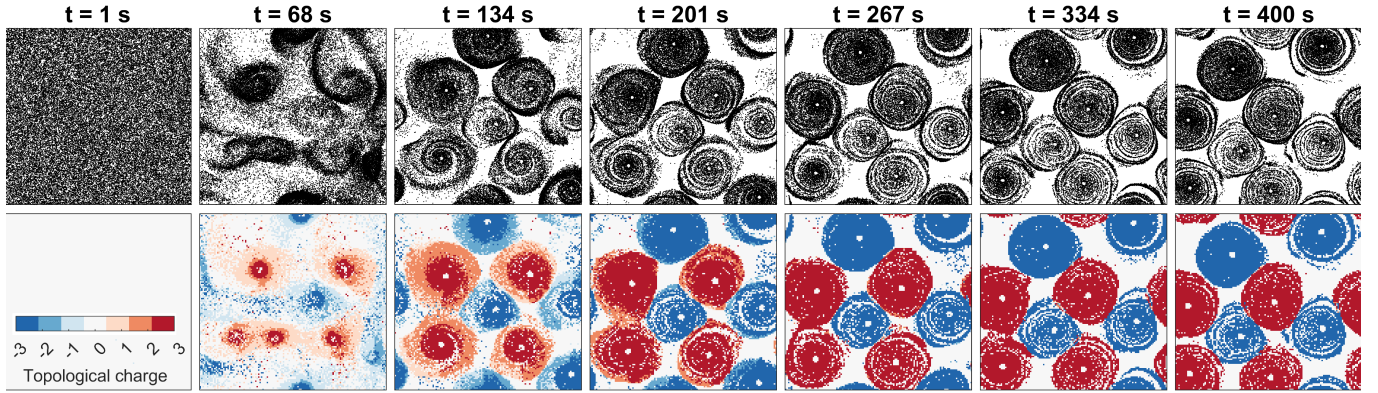


FIG. 3. **Active vortex glass** made of particles whose raw distribution features an inverse cascade ($\Pi(k) < 0$), but whose RFE field features a forward-cascade ($\Pi(k) > 0$). The defect count falls off drastically and flattens; defect merger is arrested and the ensemble settles in a frozen defect lattice. Top row shows the RFE particle point-cloud while bottom row shows topological charge, while the columns correspond to seven temporal snapshots.

TABLE I. **Thermodynamic Phases of Chiral Active Matter.** The system state is determined by the intrinsic frequency dispersion $\Delta\omega$. High activity drives the inverse cascade towards the Onsager dipole, while low activity leads to kinetic jamming (glass). Π_{Raw} and Π_{RFE} refer to spectral flux for the raw particle distribution and the RFE field respectively. See Figure 6 in the End Matter for a rigorous characterization of the three phases.

Phase	$\Delta\omega$	Micro-Physics	Macro-State	Signature
I. Global synchronisation	$\Delta\omega \rightarrow 0$	$\nabla\phi \rightarrow 0$.	Static clumps (Fig. 5).	$\Pi_{Raw} > 0, \Pi_{RFE} > 0$
II. Active Vortex Glass	Low / narrow	Frustration; no merger.	Defect solid (Fig. 3).	$\Pi_{Raw} < 0, \Pi_{RFE} > 0$
III. Onsager Condensate	High / broad	Shock merger.	Onsager dipole (Fig. 1).	$\Pi_{Raw} < 0, \Pi_{RFE} < 0$

erator (Eqs. 4, 5), essentially a low-pass filter, it may be possible to recover inertial scaling laws in a broad class of overdamped systems.

Supersonic topological gas dynamics The realization of the Onsager dipole depends strictly on the system's ability to overcome topological energy barriers [25]. As alluded to by Ref. [21], we find that the intrinsic frequency dispersion $\Delta\omega$ determines whether the topological gas freezes, jams, or flows.

Figure 3 illustrates the foregoing by presenting the evolution of a simulation that used a narrower, lower-frequency dispersion $\Delta\omega$ (see Figure 4 in the End Matter); the raw particle distribution subsequently drove an inverse cascade, but the renormalised fluid did not, and the active bath was unable to transfer energy to wavenumbers $k < k_c$, resulting in an *arrested topological defect glass state*. While the Onsager fluid exhibits continuous, power-law coarsening, the vortex glass state exhibits a rapid localized quench ($N \propto t^{-2}$) followed by a kinetic *arrest* ($N \rightarrow \text{const.}$), and static, quantized loop currents of phase information [21, 29]. This leads us to propose that the experimental 'active glass' described in Ref. [52] may be an intrinsic phase of topological gases, for which we provide an explicit theoretical foundation.

In Table I we summarize the results of varying the shape of $\Delta\omega$ (see the End Matter). This yields the stability boundaries of the topological gas dynamics and the

thermodynamic Onsager attractor, where we identify the limit $R \rightarrow 1$, leading to a ferromagnetic-like collapse.

The Onsager dipole state, which represents the hydrodynamic limit, is thus in a *marginal synchronisation regime*, meaning that the synchronising force is balanced by continuous, shock-driven thermalization of inertial energy. This is empirically confirmed by observing that the dynamics in Figure 1 effectively *never stop*. The observed density decay $N(t) \sim t^{-0.75}$ during this phase quantitatively distinguishes the regime from compressible gas dynamics ($t^{-2/3}$ or t^{-1} , [53]), favoring coherent structure merger in shallow waters [40]. The dominance of shock-mergers over smooth thinning confirms the system operates in the supersonic regime ($M > 1$), strictly isomorphic to supercritical shallow water flow, where density fluctuations map directly to hydraulic jumps [41, 43].

CONCLUSION

We have identified a disorder-induced transition in chiral active matter where a topological heat pump drives an inverse cascade, saturating in a negative-temperature, dynamic Onsager dipole, representing a hydrodynamic limit that is isomorphic with shallow water theory. This mapping reconciles dissipative microphysics with macroscopic inertial transport. Our findings suggest active matter is governed by an emergent topological inertia, offering a new paradigm for robust transport.

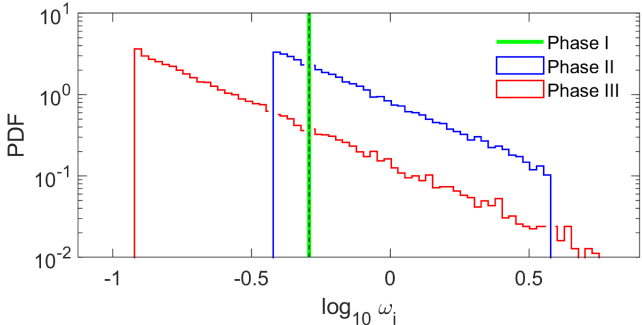


FIG. 4. The three distributions in $\Delta\omega$ corresponding to the three thermodynamic phases in Table I, showing only the positive component (ω_i is symmetric around 0). The lower limit on the x -axis is given by $(2\Lambda)^{-1}$, the hypothetical “box-size fluctuation.”

END MATTER

The *End Matter* provides the empirical and theoretical foundation for the phase diagram in Table I, through simulations that systematically vary the disorder distribution $\Delta\omega$, and concludes with some perspectives on the conceptual implications of our results.

The three thermodynamic phases of topological gas dynamics Consider the theoretical turbulence frameworks of Ref. [25] (self-organisation) and Ref. [36] (forced hydrodynamics). The former describes an active, excitable medium of interacting fluctuations capable of self-organization, wherein a complex mean field amplitude (Z) that arises from phase synchronisation acts as an effective force that traps individual stochastic oscillators into coherent clusters. The latter modeled a stable, self-similar dipole condensate that accumulates inverse-cascading energy at the system size, yielding a large-scale coherent vorticity Ω .

Before we pinpoint the conjunction between the latter two theoretical forays, we show, in Figure 4, three distributions in ω_i , corresponding to $\Delta\omega$ in Table I. Intrinsic frustration ω_i near the box-size, $(2\Lambda)^{-1}$, acts simultaneously as Z in Ref. [25] and Ω in Ref. [36]. Thus, if frustration $\Delta\omega$ is too low-valued and too narrow, the system generates active stress but lacks the transport coherence to move it, yielding an arrested glass vortex. Conversely, if the dispersion in ω_i is both sufficiently high and sufficiently broad (reaching near-box-size fluctuations), the system effectively facilitates the emergence of a space-filling Onsager dipole. In Figure 6 we rigorously demonstrate the foregoing descriptions by extracting the median results from 16 ensemble simulations of the three phases. Crucially, we observe that the spectral flux in Phase I (see Figure 5) is positive for both the raw and RFE fields, while for Phase II (Figure 6f), the flux is negative for the raw field (crossing zero at intermediate wavenumbers) and positive for the RFE field, and for Phase III the flux is consistently negative, facilitating

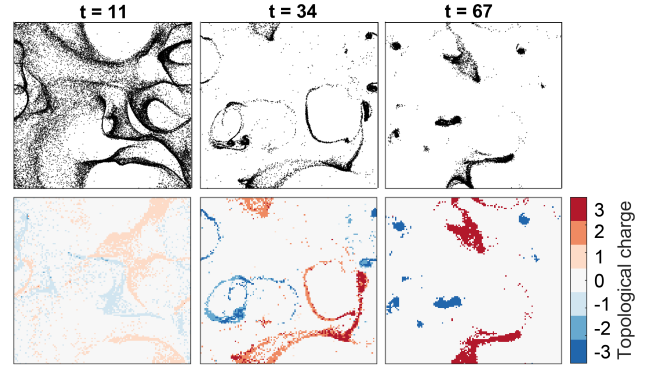


FIG. 5. **Summary of a Phase I simulation.** RFE particles as point-clouds (top row) and topological charge (bottom row) mapped with a colorscale; timestamps are indicated.

the inverse cascade that would otherwise be arrested in the case of Phase II.

Thus, the effective Euler dynamics we observe allow the system to access the condensate state. This suggests that Ref. [25]’s thermodynamic driver is strong enough in this regime to overcome the chaotic transients [16] and access Ref. [36]’s equilibrium basin. This is in contrast with the active nematic systems that often saturate in a state of defect chaos [16]. Thus, the theoretical conjunction between Ref. [25]’s extremum principles with Ref. [36]’s statistical mechanics bolsters the notion that the Onsager dipole in our simulation is a thermodynamically preferred attractor.

Future studies should map out the biological, chemical, and environmental circumstances that facilitate the emergence of an inertial flow in soft, active matter turbulence, and when such systems are dominated by low-Reynolds number friction and rapid energy decay [14–16], as well as specific instances where the theoretical foundations for our hydrodynamic limit breaks down.

The potential reach of supersonic topological gas dynamics In the biological microscopic realm, large-scale mixing is vital for nutrient transport [54]. Conceptually, our model suggests that a biological system benefits from a specific variance in intrinsic traits (modeled as the dispersion $\Delta\omega$) to activate the topological heat pump, or revert to a defect lattice. This provides a mechanistic explanation for why phenotypic heterogeneity is prevalent [55] and suggests that such noise expressions are in fact beneficial for cohesion. Biological systems may thus inadvertently exploit noise in gene expression [56], effectively tapping into disorder as a means for macroscopic transport.

In our model, when the system is disordered ($R \rightarrow 0$), it is effectively massless and governed by overdamped diffusion. As it synchronizes, it acquires mass ($\lambda = R^2$), supporting momentum transport and waves akin to correlation propagation in flocks and swarms [14, 57], with the caveat that our system operates in two dimensions.

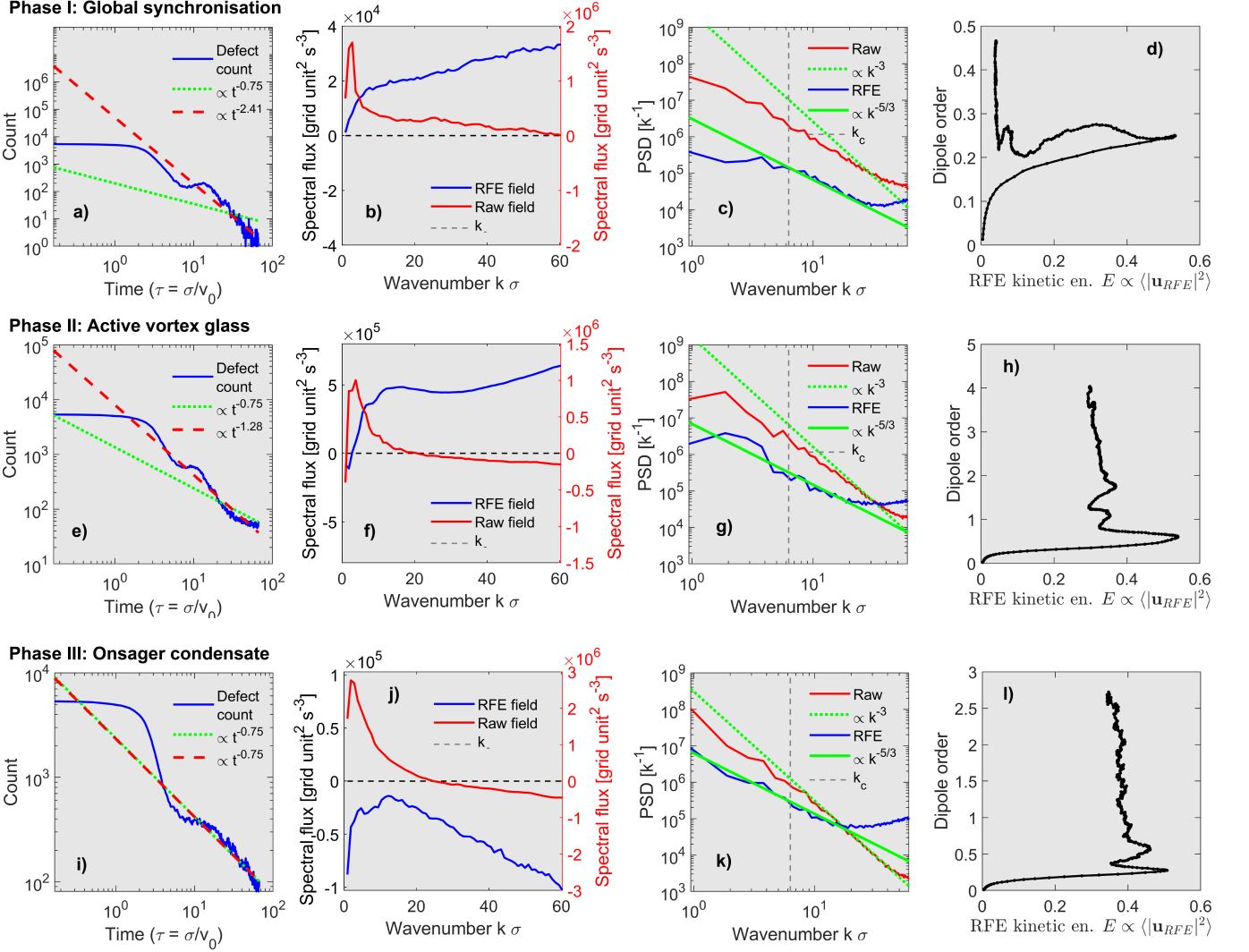


FIG. 6. **Ensemble averages of 16 simulations, showing the behaviour of the three phases in Table I.** The leftmost column (panels a, e, and i) show the defect count $N_d(t)$ in a solid blue line, with a $t^{-0.75}$ powerlaw in dotted green line and a fit for $t > 3.4$ (through non-linear minimization of root-mean square error) powerlaw in dashed red line. The next column (panels b, f, and j) show median spectral flux for the raw (red) and RFE (blue) fields. The third column (panels c, g, and k) show the energy spectrum for the raw (red) and RFE (blue) fields, with k^{-3} and $k^{-5/3}$ powerlaw fits, as well as the cut-off scale k_c . The last column (panels d, h, and l) show the thermodynamic trajectory. All quantities are shown as medians of 16 randomized (in initial locations x_i, y_i and white-noise η_i) runs.

The observed R -dependency implies that defects behave as *massless holes* (see Figure 7 in the Supplementary Materials) in an otherwise massive fluid. This mass contrast enables a supersonic topological gas dynamic: defects accelerate across phase gradients faster than the bulk sound speed [58], maintaining scale-free coherence [59] without central processing.

In the field of robotics, heterogeneity is usually considered a manufacturing error. For example, the Kuramuro model describes the superconductor-to-insulator transition (or Bose Metal state) in *dirty Josephson arrays*, quantum oscillator systems that feature synchronisation due to fabrication imperfections [24, 60], to which

the transition between Phases II and III in Table I is (classically and locally) analogous. This heterogeneity, which typically cannot be avoided, can potentially be exploited as a control input [44, 61]. For example, in smart materials, the Phase II-III transition can be achieved by electromagnetic field-control of rotors, enabling shock-absorption (converting kinetic energy temporarily into topological sorting; see also Refs. [62, 63]). With attention to edge-effects, microfluidic applications could involve an “Onsager valve” with zero moving parts and negative effective viscosity, acting both as valve and pump, depending on control input (see Ref. [64]).

SUPPLEMENTARY MATERIALS: DERIVATION OF THE HYDRODYNAMIC LIMIT

In this section, we derive the hydrodynamic limit of our model, beginning with deriving the macroscopic velocity, the advective transport term for the model, and establishing an analogy with shallow water hydrodynamics, providing closure to the argument that active chiral matter can exhibit Euler turbulence. We note that we reinstate the units in this section to track dimensional consistency.

Velocity and continuity

We define the macroscopic velocity field $\mathbf{u}(\mathbf{r}, t)$ as the local average of the particle velocities. Decomposing the particle phase into the local mean phase Ψ and a fluctuation $\delta\phi_i$ (that is, $\phi_i = \Psi + \delta\phi_i$), and assuming symmetric fluctuations (that is, $\langle \sin \delta\phi \rangle \approx 0$), the coarse-grained velocity becomes,

$$\mathbf{u} = \langle \mathbf{v}_i \rangle \approx v_0 \langle \cos \delta\phi \rangle (\cos \Psi, \sin \Psi). \quad (13)$$

We identify the local order parameter R_1 ,

$$R_n = \langle \cos(n\delta\phi) \rangle = \text{Re} [\langle e^{in\delta\phi} \rangle], \quad (14)$$

for a peaked (narrow) Gaussian distribution in $\delta\phi$; we then drop the subscript. R measures the degree of local synchronisation. Thus, we obtain,

$$|\mathbf{u}| = v_0 R. \quad (15)$$

While individual particles move at constant speed v_0 , the renormalised fluid element speed is variable and proportional to the local synchronisation. To express \mathbf{u} in terms of the mean field Ψ , we identify the flow direction $\hat{\mathbf{n}} = (\cos \Psi, \sin \Psi)$ with the normalized phase gradient:

$$\mathbf{u} = v_0 R \frac{\nabla \Psi}{|\nabla \Psi|}. \quad (16)$$

Eq. (16) is globally valid: at defect cores where the phase Ψ is undefined, the order parameter vanishes ($R \rightarrow 0$), ensuring the velocity field remains continuous and bounded ($\mathbf{u} \rightarrow 0$). Recognizing that $\nabla \Psi$ scales as $1/r$ near defects, we note that the vector \mathbf{u} is parallel to $\nabla \Psi$. Far from defect cores, where the phase gradient magnitude varies slowly ($|\nabla \Psi| \approx \text{const}$), the flow simplifies to an effective potential flow:

$$\mathbf{u} \approx R \nabla \Psi. \quad (17)$$

This approximation eventually allows us to utilize the machinery of inviscid fluid mechanics in the bulk of the domain, while the factor R naturally regularizes the dynamics at the topological singularities.

Before providing closure to the above, we need to address continuity. The continuity equation for \mathbf{u} then reads,

$$\frac{\partial \rho}{\partial t} + \nabla \cdot (\rho \mathbf{u}) = 0. \quad (18)$$

Substituting Eq. (17) into Eq. (18), we observe that the macroscopic density evolution is governed by mean phase curvature:

$$\frac{\partial \rho}{\partial t} \approx -v_0 R \nabla \cdot (\rho \nabla \Psi). \quad (19)$$

This formulation identifies the system as formally analogous to the shallow water equations [65, 66], where the active density ρ acts as the fluid height (see Appendix-subsection). The phase curvature $\nabla^2 \Psi$ drives the compression of the fluid elements, explicitly linking topological defects to density fluctuations.

Eq. (9) implies $|\nabla \Psi| = m/r$. Substituting this into our macroscopic velocity definition (Eq. 16), and assuming the order parameter R is *locally* uniform, the fluid velocity induced by a defect scales as:

$$|\mathbf{u}| \approx v_0 R \frac{m}{r}. \quad (20)$$

This confirms that the topological defects of the mean phase act as point vortices with an effective physical circulation $\Gamma \approx 2\pi m v_0 R$. Consequently, we arrive at the Kirchhoff-Onsager Hamiltonian in Eq. (10). Crucially, this derivation highlights that the topological charge driving the Hamiltonian dynamics is scaled by the order parameter R . If renormalization (or synchrony) is suppressed ($R \rightarrow 0$), the effective circulation vanishes ($\Gamma_{\text{eff}} \rightarrow 0$), causing the Hamiltonian interaction to collapse.

Momentum and Pressure

We start with the discrete, slaved velocity,

$$\mathbf{v}_i = v_0 (\cos \phi_i, \sin \phi_i).$$

We define a momentum density field $\mathbf{g}(\mathbf{r}, t)$, which in the discrete case becomes,

$$\mathbf{g}(\mathbf{r}, t) = \sum_{i=1}^N \mathbf{v}_i(t) \delta(\mathbf{r} - \mathbf{r}_i(t)), \quad (21)$$

where $\delta(x)$ now defines the Dirac delta function. Next, take the time derivative $\partial_t \mathbf{g}$,

$$\frac{\partial \mathbf{g}}{\partial t} = \underbrace{\sum_i \dot{\mathbf{v}}_i \delta(\mathbf{r} - \mathbf{r}_i)}_{\text{Orientation}} + \underbrace{\sum_i \mathbf{v}_i \frac{\partial}{\partial t} \delta(\mathbf{r} - \mathbf{r}_i)}_{\text{Transport} \equiv \mathcal{T}}, \quad (22)$$

where we identify the orientation term by noting that $\dot{\mathbf{v}}_i$ contains the Kuramoto-like phase dynamics (Eq. 2). The second term is identified as momentum transport by the chain-rule property of the delta function, delta function $\partial_t \delta(\mathbf{r} - \mathbf{r}_i) = -\nabla \cdot (\dot{\mathbf{r}}_i \delta)$, as well as noting that $\dot{\mathbf{r}}_i = \mathbf{v}_i$,

$$\mathcal{T} = -\nabla \cdot \left(\sum_i \mathbf{v}_i \mathbf{v}_i \delta(\mathbf{r} - \mathbf{r}_i) \right). \quad (23)$$

Simplifying the notation, we write,

$$\mathcal{T} = -\nabla \cdot \langle \mathbf{v}_i \mathbf{v}_i \rangle. \quad (24)$$

To see how Eq. (24) gives us an advective term $(\mathbf{u} \cdot \nabla) \mathbf{u}$, we must calculate the Tensor $\langle \mathbf{v} \mathbf{v} \rangle$. Consider the outer product $\mathbf{v}_k \mathbf{v}_k$ and average it; specifically, the components (e.g., xx):

$$\langle v_x v_x \rangle = v_0^2 \langle \cos^2(\Psi + \delta\phi) \rangle, \quad (25)$$

using the expansion of ϕ_i as a perturbation to the mean field. Using trigonometric identities and averaging over the fluctuations, we get,

$$\langle v_x v_x \rangle \approx \frac{v_0^2}{2} [1 + \underbrace{\langle \cos(2\delta\phi) \rangle}_{R_2} \cos(2\Psi)]. \quad (26)$$

where we identify the second-order order parameter $R_2 \approx R^4$ (again assuming a peaked distribution), yielding an expression for *microscopic* stress. In the fluid phase (the Onsager dipole, Phase III), where the system exhibits marginal synchronisation ($0 < R < 1$), the fluctuations are dominated by frustration ω_i , distinct from, and in opposition to, the synchronisation forces that maintain R .

For the equivalent expression for macroscopic stress, we use the definition of macroscopic velocity (Eq. 15),

$$u_x u_x = (v_0 R \cos \Psi)^2 = v_0^2 R^2 \cos^2 \Psi \quad (27)$$

Trigonometry again allows us to isolate the anisotropic part,

$$u_x u_x = \frac{v_0^2 R^2}{2} [1 + \cos(2\Psi)]. \quad (28)$$

To relate the foregoing to the hydrodynamic equations, we compare the microscopic and macroscopic tensors. In order to do so, we posit a constitutive relation of the form $\langle v_i v_j \rangle = P_{\text{eff}} \sigma_{ij} + \lambda u_i u_j$, where λ scales the advective term. Substituting the expansions from Eqs. (26) and (28) into this ansatz for the xx -component yields:

$$\underbrace{\frac{v_0^2}{2} + \frac{v_0^2 R^4}{2} \cos(2\Psi)}_{\text{Microscopic}} = \underbrace{P_{\text{eff}} + \lambda \left[\frac{v_0^2 R^2}{2} + \frac{v_0^2 R^2}{2} \cos(2\Psi) \right]}_{\text{Macroscopic Closure}}. \quad (29)$$

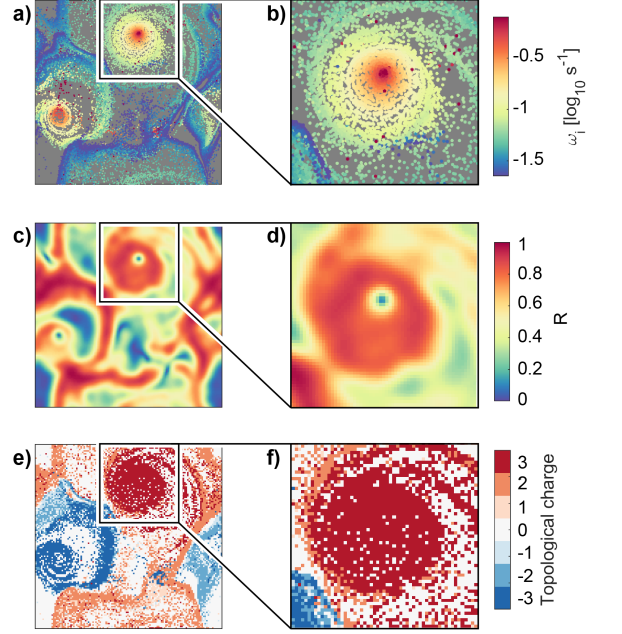


FIG. 7. The end-state of a Phase III (Onsager dipole) simulation, showing RFE particle locations, with colorscale denoting intrinsic frequency or frustration ω_i (panels a, b), the degree of local synchronization R (panels c, d), and the topological charge (panels e, f). The right column shows a blown-up portion of the left column.

Matching the *anisotropic* coefficients (the $\cos(2\Psi)$ terms) determines the coherence coefficient:

$$\frac{v_0^2 R^4}{2} = \lambda \frac{v_0^2 R^2}{2} \implies \lambda = R^2, \quad (30)$$

confirming that the *effective inertial mass* λ scales with the square of the order parameter.

It is pertinent to compare this result to the swim pressure derived in the kinetic theory of active fluids (e.g., [67]). In standard active fluids, the particle mass is constant (corresponding to $\lambda = 1$), meaning the coherent kinetic energy scales as $u^2 \propto R^2$. In our topological gas, the effective inertial mass *itself depends on local synchronisation* ($\lambda = R^2$), causing the “coherent energy” to scale as $\lambda u^2 \propto R^4$.

Next, we substitute the closure back into the momentum conservation equation and obtain,

$$\frac{\partial \mathbf{u}}{\partial t} + \lambda \nabla \cdot (\mathbf{u} \mathbf{u}) = -\nabla P_{\text{eff}} + \mathbf{F}_{\text{active}}, \quad (31)$$

where we, for the time being, leave the exact nature of $\mathbf{F}_{\text{active}}$ ambiguous, as we must first establish the specific hydrodynamic analogy.

Shallow waters and the active enthalpy functional

As stated in the Methodology section, the interpretation of Eq. (19) identifies the system being modeled as

isomorphic to the shallow water framework, where the active density ρ acts as the fluid height. To proceed, we shall use the active enthalpy functional as a theoretical vehicle [68, 69]. However, we must first bolster the connection with a specific empirical observation. Figure 7 shows the end-state of a Onsager dipole simulation, color-coding ω_i (top), R (middle), and topological charge m (bottom). We make two important observations;

(1) As alluded to in the Main Paper, ω_i in Figure 7a, b) is effectively segregated into distinct bands and regions. Because of the segregation, the local average $\langle \omega_i \rangle$ at a position \mathbf{r} becomes non-random and stable over timescales relevant to the flow. We can effectively “smear” the discrete particles into a continuous background field where $\omega(\mathbf{r}) \approx \langle \omega_i \rangle_{\mathbf{r}}$.

(2) Figure 7a–d) present clear, unambiguous empirical evidence for the fact that, at topological defect cores, $R \rightarrow 0$ and $\omega_i \gg \bar{\omega}$, validating Eq. (16) and other instances where the mean field Ψ appears in the numerator. As we shall motivate below, the conditions at defect cores implies the fluid is stiff. The flow must immediately adjust to the *topography* defined by $\omega(\mathbf{r})$. The segregation of the active particles constitutes the a potential $\Phi(\mathbf{r})$ that forces the flow.

Having motivated a conceptual shift from a Lagrangian to an Eulerian perspective, we define the effective fluid density as $\rho(\mathbf{r}, t) \equiv R(\mathbf{r}, t)^2$. We then use $\omega(\mathbf{r})$ as an external scalar potential produced by intrinsic frequency mismatch $\omega_i - \bar{\omega}$, $\bar{\omega}$ being mean frequency, the ensemble average of which equals dispersion $\Delta\omega$.

The total potential energy density \mathcal{U}_{tot} is composed of the internal interaction energy (barotropic fluid self-interaction, or non-linear coupling in turbulence physics), and the external topographic energy [70]. We have,

$$\mathcal{U}_{\text{tot}}[\rho] = \underbrace{g_{\text{eff}}/2(\rho - \rho_0)^2}_{\text{Interaction}} + \underbrace{\gamma\rho \cdot \omega(\mathbf{r})}_{\text{Topography}}, \quad (32)$$

where g_{eff} is the effective coupling constant representing the stiffness of the order parameter (analogous to gravity g in shallow waters), and γ is a coupling coefficient with dimensions length²time⁻¹ relating frequency disorder $\omega(\mathbf{r})$ to potential energy. Two concise observations can now be had by dimensional analysis. (1) the units of γ naturally lead to the definition $\gamma = \sigma v_0$, anchoring the topographic potential to the physical interaction scale of the agents. (2) by direct comparison between Eqs. (??) and (32), we observe that $g_{\text{eff}} \equiv v_0^2/2$.

Next, the force per unit mass (acceleration) acting on a fluid element is the negative gradient of the variational derivative of the energy with respect to density [70]:

$$\mathbf{F}_{\text{active}} = -\nabla \left(\frac{\delta \mathcal{U}_{\text{tot}}}{\delta \rho} \right). \quad (33)$$

Substituting Eq. (32) with ,

$$\frac{\delta \mathcal{U}_{\text{tot}}}{\delta \rho} = \frac{v_0^2}{2}(\rho - \rho_0) + \sigma v_0 \omega(\mathbf{r}). \quad (34)$$

Thus, the force field becomes,

$$\mathbf{F}_{\text{active}} = - \underbrace{v_0^2 \nabla \rho / 2}_{\text{Barotropic Pressure}} - \underbrace{\sigma v_0 \nabla \omega(\mathbf{r})}_{\text{Disorder Gradient}}, \quad (35)$$

where we note that $\nabla \omega$ appears as a conservative force field, akin to topographic steering in shallow waters [70], and in adaptations to active nematics [64]. Next, we will insert this force into the corrected Eulerian momentum equation for \mathbf{u} ,

$$\frac{D\mathbf{u}}{Dt} + (\mathbf{u} \cdot \nabla) \mathbf{u} = \mathbf{F}_{\text{active}} + \mathbf{F}_{\text{visc}}, \quad (36)$$

where we include a viscous force term \mathbf{F}_{visc} for completeness, to be addressed later. Substituting $\rho = R^2$ and our derived force, we obtain,

$$\frac{D\mathbf{u}}{Dt} = -\frac{v_0^2}{2} \nabla(R^2) - \sigma v_0 \nabla \omega(\mathbf{r}) + \nu \nabla^2 \mathbf{u}, \quad (37)$$

where $\nu \nabla^2 \mathbf{u}$ is the viscous term, and where we identified the operator D/Dt in Eq. (36), the material, or total, derivative [71]. This equation now mathematically represents a fluid flowing over a variable topography,

$$Z(\mathbf{r}) = \frac{2\sigma}{v_0} \omega(\mathbf{r}), \quad (38)$$

succinctly on display in Figure 7. Since the inertial flow necessarily moves the distribution of ω_i , the system is effectively advecting its own boundary conditions; the active particles produce the seafloor which provides topographic steering to the emergent inertial flow.

Active acoustic speed

At this point, we must address acoustics, as a shallow water vortex diffuses into the medium through sound waves. To demonstrate why our Onsager dipole is unable to do so, we first revisit the continuity and momentum equations (Eqs. 18 and 36) using $\rho = R^2$,

$$\frac{\partial(R^2)}{\partial t} + \nabla \cdot (R^2 \mathbf{u}) = 0, \quad (39)$$

and

$$\frac{\partial \mathbf{u}}{\partial t} + (\mathbf{u} \cdot \nabla) \mathbf{u} = -\frac{v_0^2}{2} \nabla(R^2) - v_0 \sigma \nabla \omega(\mathbf{r}). \quad (40)$$

To find the speed of acoustic waves, we linearize the system around a base state of constant synchronization

$R_0(\mathbf{r})$ and zero velocity, neglecting the external topography $\omega(\mathbf{r})$ to isolate the acoustic modes,

$$\mathbf{R}(\mathbf{r}, t) = R_0(\mathbf{r}) + \delta R(\mathbf{r}, t) \quad (41)$$

and $\mathbf{u} = \mathbf{v}$ (\mathbf{v} being a small perturbation). The linearized continuity and momentum equations then read,

$$\frac{\partial \delta R(\mathbf{r}, t)}{\partial t} + \frac{R_0(\mathbf{r})}{2} \nabla \cdot \mathbf{v} = 0, \quad (42)$$

and

$$\frac{\partial \mathbf{v}}{\partial t} = -v_0^2 R_0(\mathbf{r}) \nabla \delta R(\mathbf{r}, t), \quad (43)$$

respectively. Combining these by taking the time derivative of the continuity equation and substituting the momentum equation yields the wave equation:

$$\frac{\partial^2 \delta R(\mathbf{r}, t)}{\partial t^2} - \frac{v_0^2 R_0(\mathbf{r})^2}{2} \nabla^2 \delta R(\mathbf{r}, t) = 0, \quad (44)$$

from which we identify the active acoustic speed c_s ,

$$c_s(R) = \frac{v_0 R_0(\mathbf{r})}{\sqrt{2}}. \quad (45)$$

In other words, the sound-speed, or, in our case, propagation speed of oscillator state information, depends linearly on the local synchronisation R . When an acoustic wave travels from an ordered region ($R \approx 1$) into a disordered region ($R \approx 0$), a shock front necessarily forms, since the sound-speed rapidly decreases. The Mach number (M) of the flow, which is defined as the ratio of flow speed to sound speed, becomes,

$$M = \frac{|\mathbf{u}|}{c_s} \approx \frac{v_0 R}{v_0 R_0 / \sqrt{2}} = \sqrt{2} \left(1 + \frac{\delta R}{R_0} \right), \quad (46)$$

by merit of Eqs. (15) and (45). The macroscopic flow is therefore inherently supersonic ($M > 1$). Near a defect, however, $R \rightarrow 0$, and so $c_s \rightarrow 0$; state information cannot escape a defect core, turning the latter into sonic black holes. This implies the existence of a “sonic horizon” around defect cores, which become isolated behind Mach cones. Hence, defect cores cannot diffuse into their surroundings by radiating sound (such as geophysical vortices), justifying our application of the the point-vortex Onsager-Kirchoff Hamiltonian.

Figure 8 demonstrates the foregoing in empirical terms, showing the interplay between flow (panel a) and shock ridges (panel b) for the end-state of a Phase III (Onsager dipole) simulation. We observe that (1) the acoustic speed (colorscale in panel a) goes to zero near the defect cores, capturing the sonic black holes that are protected by Mach cones, and (2) the synthetic schlieren plot [72] indicates the presence of shocks that radiate outward from the defect cores, where they thermalize inertial mass R^2 .

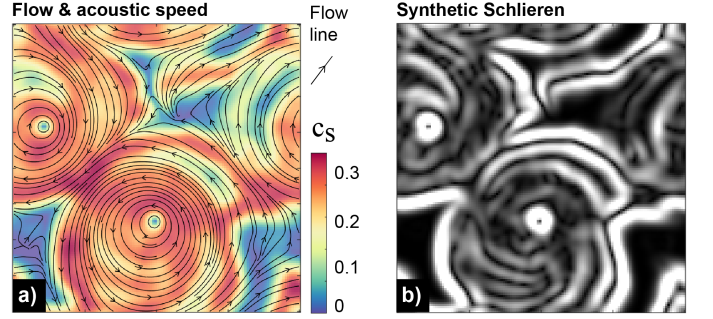


FIG. 8. **Panel a)** shows acoustic speed (Eq. 45) with a colormap, with \mathbf{u} overlaid with flow lines, for an end-state simulation space. **Panel b)** shows a synthetic Schlieren plot ($|\nabla \rho| = |\nabla R^2|$), showing shock ridges.

We are now in a position to elucidate the dynamic behaviour observed in the hydrodynamic limit of our model. The vortex merging that we observe in Figures 2 and 6, evidenced by the $t^{-0.75}$ scaling of the defect count, is explained by *shock merging* in the hydrodynamic limit. That is, when two synchronisation shocks collide, R decreases; the inertial energy contained in R^2 must be dissipated at the shock, going back into the active bath at the long-range strain interface between the defects. The active bath again synchronises, increasing R and thereby creating inertial advection, creating the remarkably stable dynamics of the Onsager dipole.

To bolster the foregoing description, we must go back to Eq. (41), we note that $\delta R(\mathbf{r}, t)$ is a fast, zero-mean fluctuation $\langle \delta R \rangle_t = 0$. We then linearise the density field R^2 :

$$R(\mathbf{r}, t)^2 = R_0(\mathbf{r})^2 + 2R_0(\mathbf{r})\delta R(\mathbf{r}, t) + (\delta R(\mathbf{r}, t))^2. \quad (47)$$

When we apply the time-average operator $\langle \cdot \rangle_t$ to this equation, the linear fluctuation term vanishes, and we are left with $\langle R^2 \rangle_t \approx R_0(\mathbf{r})^2$.

Next, we define the active velocity potential (or macroscopic phase) $\Theta(\mathbf{r}, t)$ [63],

$$\Theta(\mathbf{r}, t) = \bar{\Theta}(\mathbf{r}, t) + \delta \Theta(\mathbf{r}, t), \quad (48)$$

where a Helmholtz decomposition yields slow topological rotation (vortices) and the fast compressional vibration (acoustic waves). Our goal is to show that the slow-mode is incompressible, yielding the stable Euler dynamics that we observe in the main paper. $\delta \Theta$ describes the irrotational phase oscillations associated with the sound waves δR , and likewise time-average to zero: $\langle \delta \Theta \rangle_t = 0$. We substitute both expansions into the continuity equation,

$$\partial_t R(\mathbf{r}, t)^2 + \nabla \cdot (R(\mathbf{r}, t)^2 \nabla \Theta(\mathbf{r}, t)) = 0, \quad (49)$$

and time-average,

$$\nabla \cdot ((R_0(\mathbf{r})^2 + 2R_0(\mathbf{r})\delta R(\mathbf{r}, t)) \nabla (\bar{\Theta}(\mathbf{r}, t) + \delta \Theta(\mathbf{r}, t)))_t \approx 0. \quad (50)$$

After expanding Eq. (50), the second and third terms vanish by merit of the time-averaging, while the fourth term vanish as $\delta R(\mathbf{r}, t)$ and $\nabla \delta \Theta(\mathbf{r}, t)$ are uncorrelated. We are then left with the first dominant term, and recover the elliptic constraint for the vortex phase $\bar{\Theta}$ on the background R_0 ,

$$\nabla \cdot (R_0^2 \nabla \bar{\Theta}) = 0, \quad (51)$$

where we drop spatial and temporal dependencies for brevity. Eq. (51) describes an incompressible potential flow in a medium with variable density R_0^2 , and is analogous to the rigid lid approximation [63]. We recognise a stable Euler fluid with inertial mass R_0^2 , flowing around defect cores, and Eq. (51) enforce mass conservation for the inertial background flow.

To address the physical nature of the background flow (which, at present, remains a static field approximation), we note that while the external topography $\omega(\mathbf{r})$ was neglected to isolate the fast acoustic modes (δR), it remains the governing factor for the slow background state $R_0(\mathbf{r})$. The static balance of the active enthalpy functional (Eq. 32) dictates that $R_0(\mathbf{r})^2$ is spatially anti-correlated with $\omega(\mathbf{r})$, such that high-disorder regions create the density depressions (vacuums) that isolate defects, while low-disorder regions support the high-density ($R_0 \approx 1$) inertial fluid. A close examination of Figure 7b, d) provides clear empirical evidence for this position.

Hydrodynamic closure

As the active acoustic speed (Eq. 45) scales linearly with order ($c_s \propto R$), the sound speed inherently lags behind the inertial flow velocity by a constant, order unity, forcing the system into a global supersonic state with $M \approx \sqrt{2}$. As we discussed in the foregoing subsection, this condition mandates the formation of synchronization shocks (Mach cones) at defect sites, which act as the primary mechanism topological sorting (yielding Eulerian Onsager-Kirchoff dynamics in the supersonic topological gas). This leads us to assert the hazardous rigid lid incompressibility,

$$\nabla \cdot \mathbf{u} \approx 0. \quad (52)$$

The “phantom inertia” R^2 acts an Euler fluid with quantized circulation, which we demonstrate with rigour in the Main Paper. At the same time, on fast, acoustic timescales, the dynamics are dominated by compressible shock-mergers. The shocks thermalise inertial energy into the active bath, which subsequently build up order through inverse cascading entropy. The rigid lid incompressibility emerges as the rigorous time-averaged limit of the stiff, supersonic topological gas.

ACKNOWLEDGEMENTS

This work is supported by the European Space Agency’s Living Planet Grant No. 1000012348. The author is grateful to O. Nestande, D. Knudsen, PT. Jayachandran, and K. Douch for stimulating discussions. Google’s Gemini 3.0 Pro has been used for mathematical formalism and coding assistance in MATLAB.

* Also at The European Space Agency Centre for Earth Observation, Frascati, Italy; Contact: magnus.fagernes@gmail.com

- [1] H. H. Wensink, J. Dunkel, S. Heidenreich, K. Drescher, R. E. Goldstein, H. Löwen, and J. M. Yeomans, Mesoscale turbulence in living fluids, *Proceedings of the National Academy of Sciences* **109**, 14308 (2012).
- [2] I. S. Aranson, Bacterial active matter, *Reports on Progress in Physics* **85**, 076601 (2022).
- [3] R. Alert, J. Casademunt, and J.-F. Joanny, Active Turbulence, *Annual Review of Condensed Matter Physics* **13**, 143 (2022).
- [4] M. Bourgoin, R. Kervil, C. Cottin-Bizonne, F. Raynal, R. Volk, and C. Ybert, Kolmogorovian Active Turbulence of a Sparse Assembly of Interacting Marangoni Surfers, *Physical Review X* **10**, 021065 (2020).
- [5] K. Qi, E. Westphal, G. Gompper, and R. G. Winkler, Emergence of active turbulence in microswimmer suspensions due to active hydrodynamic stress and volume exclusion, *Communications Physics* **5**, 49 (2022).
- [6] D. Saintillan and M. J. Shelley, Active suspensions and their nonlinear models, *Comptes Rendus Physique Living Fluids / Fluides Vivants*, **14**, 497 (2013).
- [7] J. K. Bhattacharjee and T. R. Kirkpatrick, Activity induced turbulence in driven active matter, *Physical Review Fluids* **7**, 034602 (2022).
- [8] J. Urzay, A. Doostmohammadi, and J. M. Yeomans, Multi-scale statistics of turbulence motorized by active matter, *Journal of Fluid Mechanics* **822**, 762 (2017).
- [9] A. Doostmohammadi, J. Ignés-Mullol, J. M. Yeomans, and F. Sagués, Active nematics, *Nature Communications* **9**, 3246 (2018).
- [10] V. Bratanov, F. Jenko, and E. Frey, New class of turbulence in active fluids, *Proceedings of the National Academy of Sciences* **112**, 15048 (2015).
- [11] L. Giomi, Geometry and Topology of Turbulence in Active Nematics, *Physical Review X* **5**, 031003 (2015).
- [12] J. Mecke, J. O. Nketsiah, R. Li, and Y. Gao, Emergent phenomena in chiral active matter, *National Science Open* **3**, 20230086 (2024).
- [13] M. T. Reeves, T. P. Billam, B. P. Anderson, and A. S. Bradley, Inverse Energy Cascade in Forced Two-Dimensional Quantum Turbulence, *Physical Review Letters* **110**, 104501 (2013).
- [14] J. Toner and Y. Tu, Flocks, herds, and schools: A quantitative theory of flocking, *Physical Review E* **58**, 4828 (1998).
- [15] H. H. Wensink and H. Löwen, Emergent states in dense systems of active rods: From swarming to turbulence, *Journal of Physics: Condensed Matter* **24**, 464130 (2012).

[16] L. Giomi, M. J. Bowick, X. Ma, and M. C. Marchetti, Defect Annihilation and Proliferation in Active Nematics, *Physical Review Letters* **110**, 228101 (2013).

[17] M. Marmol, E. Gachon, and D. Faivre, Colloquium: Magnetotactic bacteria: From flagellar motor to collective effects, *Reviews of Modern Physics* **96**, 021001 (2024).

[18] A. Maitra, Activity Unmasks Chirality in Liquid-Crystalline Matter, *Annual Review of Condensed Matter Physics* **16**, 275 (2025).

[19] V. Vijayan, K. K., S. J. J., and P. R., From disorder to design: Entropy-driven self-organization in an agent based swarming model and pattern formation, *Chaos, Solitons & Fractals* **200**, 116894 (2025).

[20] T. Markovich and T. C. Lubensky, Chiral active fluids: Insights from the total momentum, *Physical Review E* **112**, 035409 (2025).

[21] M. F. Ivarsen, Spectral density characteristics of self-organized structuring in phase-synchronized oscillator ensembles (2025), arXiv:2508.21012 [physics].

[22] L. Onsager, Statistical hydrodynamics, *Il Nuovo Cimento (1943-1954)* **6**, 279 (1949).

[23] J. A. Acebrón, L. L. Bonilla, C. J. Pérez Vicente, F. Ritort, and R. Spigler, The Kuramoto model: A simple paradigm for synchronization phenomena, *Reviews of Modern Physics* **77**, 137 (2005).

[24] F. De Smet and D. Aeyels, Partial entrainment in the finite Kuramoto–Sakaguchi model, *Physica D: Nonlinear Phenomena* **234**, 81 (2007).

[25] M. Y. Marov and A. V. Kolesnichenko, Self-Organization of Developed Turbulence and Formation Mechanisms of Coherent Structures, in *Turbulence and Self-Organization: Modeling Astrophysical Objects*, edited by M. Y. Marov and A. V. Kolesnichenko (Springer, New York, NY, 2013) pp. 373–423.

[26] K. K. Dey, Dynamic Coupling at Low Reynolds Number, *Angewandte Chemie International Edition* **58**, 2208 (2019).

[27] N. D. Mermin, The topological theory of defects in ordered media, *Reviews of Modern Physics* **51**, 591 (1979).

[28] L. M. Pismen, *Vortices in Nonlinear Fields: From Liquid Crystals to Superfluids, from Non-Equilibrium Patterns to Cosmic Strings*, Vol. 100 (Oxford University Press, 1999).

[29] R. Delabays, T. Coletta, and P. Jacquod, Multistability of phase-locking and topological winding numbers in locally coupled Kuramoto models on single-loop networks, *Journal of Mathematical Physics* **57** (2016).

[30] Y. N. Ovchinnikov and I. M. Sigal, The energy of Ginzburg–Landau vortices, *European Journal of Applied Mathematics* **13**, 153 (2002).

[31] D. E. Pelinovsky and P. G. Kevrekidis, Variational approximations of trapped vortices in the large-density limit, *Nonlinearity* **24**, 1271 (2011).

[32] M. E. Cates and J. Tailleur, Motility-Induced Phase Separation, *Annual Review of Condensed Matter Physics* **6**, 219 (2015).

[33] R. H. Kraichnan, Inertial-range transfer in two- and three-dimensional turbulence, *Journal of Fluid Mechanics* **47**, 525 (1971).

[34] V. Borue, Spectral exponents of enstrophy cascade in stationary two-dimensional homogeneous turbulence, *Physical Review Letters* **71**, 3967 (1993).

[35] V. Borue, Inverse energy cascade in stationary two-dimensional homogeneous turbulence, *Physical Review Letters* **72**, 1475 (1994).

[36] M. Chertkov, C. Connaughton, I. Kolokolov, and V. Lebedev, Dynamics of Energy Condensation in Two-Dimensional Turbulence, *Physical Review Letters* **99**, 084501 (2007).

[37] A. N. Kolmogorov, LOCAL STRUCTURE OF TURBULENCE IN AN INCOMPRESSIBLE VISCOUS FLUID AT VERY HIGH REYNOLDS NUMBERS, *Soviet Physics Uspekhi* **10**, 734 (1968).

[38] G. F. Carnevale, J. C. McWilliams, Y. Pomeau, J. B. Weiss, and W. R. Young, Evolution of vortex statistics in two-dimensional turbulence, *Physical Review Letters* **66**, 2735 (1991).

[39] S. B. Pope, *Turbulent Flows* (Cambridge: Cambridge University Press, 2000).

[40] V. D. Larchev and J. C. McWilliams, Weakly decaying turbulence in an equivalent-barotropic fluid, *Physics of Fluids A: Fluid Dynamics* **3**, 938 (1991).

[41] M. A. Hoefer, M. J. Ablowitz, I. Coddington, E. A. Cornell, P. Engels, and V. Schweikhard, Dispersive and classical shock waves in Bose-Einstein condensates and gas dynamics, *Physical Review A* **74**, 023623 (2006).

[42] A. V. Gurevich and L. P. Pitaevskii, Nonstationary structure of a collisionless shock wave, *Zhurnal Eksperimentalnoi i Teoreticheskoi Fiziki* **65**, 590 (1973).

[43] W. G. Unruh, Experimental Black-Hole Evaporation?, *Physical Review Letters* **46**, 1351 (1981).

[44] S. Shankar, A. Souslov, M. J. Bowick, M. C. Marchetti, and V. Vitelli, Topological active matter, *Nature Reviews Physics* **4**, 380 (2022).

[45] J. G. Esler, Equilibrium energy spectrum of point vortex motion with remarks on ensemble choice and ergodicity, *Physical Review Fluids* **2**, 014703 (2017).

[46] T. Tanogami and S.-i. Sasa, A Simple XY Model for Cascade Transfer (2022), arXiv:2106.11670 [cond-mat].

[47] A. S. Bradley and B. P. Anderson, Energy Spectra of Vortex Distributions in Two-Dimensional Quantum Turbulence, *Physical Review X* **2**, 041001 (2012).

[48] M. James, W. J. T. Bos, and M. Wilczek, Turbulence and turbulent pattern formation in a minimal model for active fluids, *Physical Review Fluids* **3**, 061101 (2018).

[49] M. Linkmann, G. Boffetta, M. C. Marchetti, and B. Eckhardt, Phase Transition to Large Scale Coherent Structures in Two-Dimensional Active Matter Turbulence, *Physical Review Letters* **122**, 214503 (2019).

[50] S. Mukherjee, R. K. Singh, M. James, and S. S. Ray, Intermittency, fluctuations and maximal chaos in an emergent universal state of active turbulence, *Nature Physics* **19**, 891 (2023).

[51] K. V. Kiran, K. Kumar, A. Gupta, R. Pandit, and S. S. Ray, Onset of Intermittency and Multiscaling in Active Turbulence, *Physical Review Letters* **134**, 088302 (2025).

[52] A. Chardac, S. Shankar, M. C. Marchetti, and D. Bartolo, Emergence of dynamic vortex glasses in disordered polar active fluids, *Proceedings of the National Academy of Sciences* **118**, e2018218118 (2021).

[53] S. Kida, Asymptotic properties of Burgers turbulence, *Journal of Fluid Mechanics* **93**, 337 (1979).

[54] R. Jeanneret, D. O. Pushkin, V. Kantsler, and M. Polin, Entrainment dominates the interaction of microalgae with micron-sized objects, *Nature Communications* **7**, 12518 (2016).

[55] G. Ariel, A. Rabani, S. Benisty, J. D. Partridge, R. M. Harshey, and A. Be'er, Swarming bacteria migrate by Lévy Walk, *Nature Communications* **6**, 8396 (2015).

[56] M. Ackermann, A functional perspective on phenotypic heterogeneity in microorganisms, *Nature Reviews Microbiology* **13**, 497 (2015).

[57] D. R. Brumley, K. Y. Wan, M. Polin, and R. E. Goldstein, Flagellar synchronization through direct hydrodynamic interactions, *eLife* **3**, e02750 (2014).

[58] A. Attanasi, A. Cavagna, L. Del Castello, I. Giardina, T. S. Grigera, A. Jelić, S. Melillo, L. Parisi, O. Pohl, E. Shen, and M. Viale, Information transfer and behavioural inertia in starling flocks, *Nature Physics* **10**, 691 (2014).

[59] A. Cavagna, A. Cimarelli, I. Giardina, G. Parisi, R. Santagati, F. Stefanini, and M. Viale, Scale-free correlations in starling flocks, *Proceedings of the National Academy of Sciences* **107**, 11865 (2010).

[60] K. Wiesenfeld, New results on frequency-locking dynamics of disordered Josephson arrays, *Physica B: Condensed Matter Proceedings of the ICTP Workshop on Josephson Junction Arrays*, **222**, 315 (1996).

[61] K. P. O'Keeffe, H. Hong, and S. H. Strogatz, Oscillators that sync and swarm, *Nature Communications* **8**, 1504 (2017).

[62] A. J. Liu and S. R. Nagel, Jamming is not just cool any more, *Nature* **396**, 21 (1998).

[63] M. C. Marchetti, J. F. Joanny, S. Ramaswamy, T. B. Liverpool, J. Prost, M. Rao, and R. A. Simha, Hydrodynamics of soft active matter, *Reviews of Modern Physics* **85**, 1143 (2013).

[64] K. Thijssen, D. A. Khaladj, S. A. Aghvami, M. A. Gharbi, S. Fraden, J. M. Yeomans, L. S. Hirst, and T. N. Shendruk, Submersed micropatterned structures control active nematic flow, topology, and concentration, *Proceedings of the National Academy of Sciences* **118**, e2106038118 (2021).

[65] W. Y. Tan, *Shallow Water Hydrodynamics: Mathematical Theory and Numerical Solution for a Two-dimensional System of Shallow-water Equations* (Elsevier, 1992).

[66] C. B. Vreugdenhil, *Numerical Methods for Shallow-Water Flow* (Springer Science & Business Media, 2013).

[67] S. C. Takatori, W. Yan, and J. F. Brady, Swim Pressure: Stress Generation in Active Matter, *Physical Review Letters* **113**, 028103 (2014).

[68] R. Zhang, Y. Zhou, M. Rahimi, and J. J. de Pablo, Dynamic structure of active nematic shells, *Nature Communications* **7**, 13483 (2016).

[69] S. S. Turzi, Active nematic gels as active relaxing solids, *Physical Review E* **96**, 052603 (2017).

[70] R. Salmon, *Lectures on Geophysical Fluid Dynamics* (Oxford University Press, 1998).

[71] Y. Kuramoto, *Chemical Oscillations, Waves, and Turbulence* (Courier Corporation, 2003).

[72] G. S. Settles, *Schlieren and Shadowgraph Techniques: Visualizing Phenomena in Transparent Media* (Springer Science & Business Media, 2001).